Polarization image laser line extraction methods for reflective metal surfaces

Jaime Marco-Rider, Andrej Cibicik, Olav Egeland

***Abstract*— In this work, we propose a novel pipeline method for laser line extraction from images with a polarization image sensor. The proposed method is specially developed for strong laser beam reflections from metal surfaces. For the pre-processing stage, we propose a demosaicing algorithm for color polarizer filter array (CPFA) sensors. This can be implemented by using either one quarter or full resolution of the sensor. In addition, we propose two methods for optimizing the information available in a 12-channel color polarization image: The first method, is based on the minimum linearly polarized irradiance, and the second method, is based on the linear polarization intensity. These pre-processing, and optimization methods are combined with laser line extraction methods. The laser line extraction is done with either the Polarized Finite Impulse Response (FIR) Center Of Gravity (COG), where the laser line coordinates are computed from the filtered laser intensity distribution, or with the Polarized FIR-Peak, where the laser line coordinates are calculated from the first derivative of the filtered laser signal. The performance of the proposed algorithms is studied experimentally using a laser line scanner assembly, made of a polarization camera, and a laser line projector operating in the blue wavelength range.**

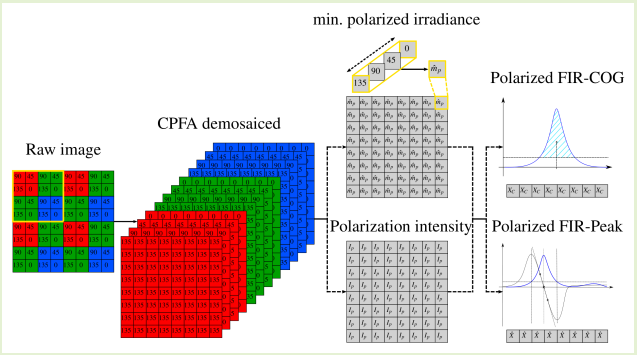

***Index Terms*— polarization imaging, polarization sensor, laser line extraction, reflective metal scanning, aluminium scanning, structured light sensor**

I. Introduction

MACHINE vision systems are extensively used in various manufacturing processes [1]. Typical applications include feedback for process control, safety systems, inspections, quality control, etc [2]. One of the most used sensor systems, for such industrial applications, is laser line scanners based on triangulation of the camera image coordinates of a projected laser line [3]. The technology is dependent on the accurate representation of the projected line geometry in the image. When laser line scanners are applied to reflective metal surfaces, laser beam reflections introduce light disturbances, which makes it difficult to accurately detect the projected line captured by the camera image [4]. Such problems are typical for, e.g., ground surfaces of welding grooves in steel [5]–[7] or aluminium [8]. Therefore, in this work we propose and study algorithms for laser line extraction from the image of a camera with a single polarization image sensor, in presence of noise caused by laser reflections.

Laser line scanners, which in general are referred to as structured light triangulation sensors, are composed of a light source, which is usually a laser projecting a beam with a known shape, in combination with a photodetector which is usually an image sensor. The two available image sensor technologies available in the market are Charged Couple Device (CCD) and Complementary metal–oxide–semiconductor (CMOS), where the CMOS image sensors (CIS) is the technology that has taken over the image sensor market [9]. As a result, most of the advances done are based on CIS technology. Although there are image sensors that operate in a spectrum with either a longer [10] or a shorter [11] wavelength than visible light, the CIS technology operating in the visible spectrum is getting the most attention from the industry [12]. As an advance in the visible spectrum CIS field, a process for fabrication of a CIS with pixel-wise on-chip polarizers was presented in [13], making the broad availability of commercial off-the-shelf polarization cameras possible.

Polarization imaging has been an active topic in the research community for decades [14]. It is normally possible by means of either rotating the polarizers manually or capturing several images simultaneously [15]. The most common imaging architecture for integrated polarimeters, which can capture several polarization images at the same time using a single image sensor, is referred to as Division of Focal plane (DoFP) [16], [17]. An image sensor fabricated using the DoFP architecture is referred to as a DoFP image sensor.

The increased availability of commercial polarization CIS

The presented work is funded by the Research Council of Norway under MAROFF Project Number 295138.

Jaime Marco-Rider and Olav Egeland are with the Dept. of Mechanical and Industrial Engineering, Norwegian University of Science and Technology (NTNU), 7034 Trondheim, Norway. (e-mail: jaime.marco@ntnu.no, olav.egeland@ntnu.no).

Andrej Cibicik is with the Dept. of Production Technology, SINTEF Manufacturing AS, 7031 Trondheim, Norway. (e-mail: andrej.cibicik@sintef.no).

cameras led to increasing research efforts which focused on the process of recovering the information from a DoFP image sensor in the most accurate way, which is generally called demosaicing. The process of reconstructing the red, blue and green channel images from a Color Filter Array (CFA) is well known in the literature [18], and it is commonly known as Bayer demosaicing. Meanwhile, the reconstruction of the four linearly polarized images is referred to as a Polarizer Filter Array (PFA) demosaicing. The combination of both, the CFA, and PFA arrangements is referred to as Colored Polarized Filter Array (CPFA) demosaicing. Both, PFA, and CPFA demosaicing are considered new techniques and are under active research [19]–[21].

In addition to the image sensor technology used in laser line scanners, the different methods to compute the position of the laser line in an image with sub-pixel accuracy is an active research topic. A commonly used method is based on intensity, and is referred to as the Center Of Gravity (COG) method, sometimes also called as Center of Mass method [22]. Some other methods include, an unbiased approach based on explicit models for lines [23], a Finite Impulse Response (FIR) filtering approach [24], or Convolutional Neural Networks [25]. An up-to-date and more in-depth review on the topic of laser line extraction can be found in [26].

As it was previously mentioned, reflections are a common problem for image sensors in general, and laser line scanners in particular, when images are captured of reflective metal surfaces. Several published strategies could potentially be used to minimize the reflections in a captured image by means of: a matte coat or sensor position planning [27]–[29], stereo cameras, or fringe projection [30], [31], lens-mounted polarizer filter, or color separation [4], [32], Time of Flight, High Dynamic Range, or motion contrast sensors [33]–[35], as well as image-based methods, or machine learning [36], [37].

Although a literature review has revealed a significant amount of research on the methods, and technologies for laser line scanners, the idea of using a polarization CIS that can mitigate the amount of reflections at sensor level, for the application to reflective metal surfaces is novel. In addition, the existing approaches for reflection reduction can introduce more complexity to the sensor system:

- Matte coating is not always technologically allowed, whereas sensor position planning can be physically restricted;
- Stereo cameras and fringe projection can result in a bulky setup;
- Polarizer and color filter mounted on the lens are additional external optical elements;
- Machine learning methods require a large teaching database and a lot of computational power.

Therefore, we propose a new approach for the extraction of a laser line from a polarization CIS image. This is a continuation of our previous work in [8]. The detailed contributions in this paper can be summed up as:

- Design of a novel laser line scanner system based on a polarization CIS that is an improvement over already existing technologies, when extracting the laser line coordinates from images of reflective surfaces;
- Two novel methods to minimize the noise of the measurements based on the unique capabilities of the polarization CIS: the first method is based on the minimum linearly polarized irradiance of the 4 linear polarization angles, and the second method is based on the linear polarization intensity, which is computed by means of the Stokes parameters;
- Two novel algorithms for extracting the laser line coordinates from an image: the Polarized FIR-COG method, and the Polarized FIR-Peak method;
- The proposed methods have been developed using basic operations (e.g., downsampling and convolution), which facilitates implementing the entire pipeline on an industrial embedded system.

The rest of this paper is organized as follows. Section II, shortly presents the preliminaries of this work. Section III, introduces the proposed polarized vision system, whereas Sections IV, and V, present the proposed algorithms for preprocessing, and optimization of color polarized image data respectively. Laser line extraction algorithms for polarized images are given in Section VI. Section VII, presents the experimental study results and discussion, whereas Section VIII, draws conclusions of this work.

II. Preliminaries

A. Polarization of light

Light exhibits a vectorial nature that can be described by polarization. The equation of the polarization ellipse can be expressed in terms of the four Stokes parameters S_0, S_1, S_2 and S_3 [38]. The Stokes parameter S_0 is the total irradiance, S_1 denotes the preponderance of horizontal polarization over vertical polarization, S_2 denotes the preponderance of 45 $\deg$ polarization over 135 $\deg$ polarization, and S_3 denotes the preponderance of the right over the left circularly polarized flux. An important property is that for any state of polarized light, the Stokes parameters satisfy the condition

$$S_0^2 \geq S_1^2 + S_2^2 + S_3^2. \tag{1}$$

The angle of polarization Ψ (or AoP) can be expressed by the Stokes parameters as

$$\Psi = \frac{1}{2} \arctan \frac{S_2}{S_1} \tag{2}$$

and the degree of polarization DoP can be expressed as

$$DoP = \frac{I_{\text{pol}}}{I_{\text{tot}}} = \frac{\sqrt{S_1^2 + S_2^2 + S_3^2}}{S_0} \tag{3}$$

where $0 \leq DoP \leq 1$, I_{tot} is the total intensity and I_{pol} is the total polarization intensity.

For more details on the theory of polarization, the reader is referred to [39].

B. Polarization image sensor

Traditional image sensors can measure the oscillations of light waves as a scalar. In order to measure the four Stokes parameters (S_0, S_1, S_2 and S_3), a full Stokes polarization camera [40] would ideally have to be used. This is due to the necessity of acquiring the four linearly polarized images (I_0, I_{45}, I_{90} and I_{135}), plus the two circularly polarized images (I_L and I_R) for the left, and right circular polarization respectively. Then, the Stokes parameters can be determined as

$$\begin{aligned} S_0 &= I_0 + I_{90}, \quad S_1 = I_0 - I_{90} \\ S_2 &= I_{45} - I_{135}, \quad S_3 = I_R - I_L \end{aligned} \tag{4}$$

The Stokes parameters (4), can also be expressed as the Stokes vector $\mathbf{S} = [S_0 \ S_1 \ S_2 \ S_3]^{\mathrm{T}}$.

The architecture of the polarization CIS used in this work [13], is designed with four linear polarizers at four different angles, whereas the two circular polarizers are missing on the hardware side. This configuration is often referred to as a Linear Stokes Polarization camera [41]. For this case, the Stokes vector is $\mathbf{S} = [S_0 \ S_1 \ S_2]^{\mathrm{T}}$. Then, DoP as defined in (3), is referred to as the degree of linear polarization $DoLP$, which is defined as

$$DoLP = \frac{I_{\mathrm{Lpol}}}{I_{\mathrm{tot}}} = \frac{\sqrt{S_1^2 + S_2^2}}{S_0} \tag{5}$$

where I_{Lpol} is the linear polarization intensity.

The polarizers used in such a polarization CIS are called wired grid polarizers, and they block (by reflection) the polarization parallel to the wire direction, whereas they transmit the polarization normal to the wire direction [13]. A representation of these polarizers can be seen in Fig. 1.

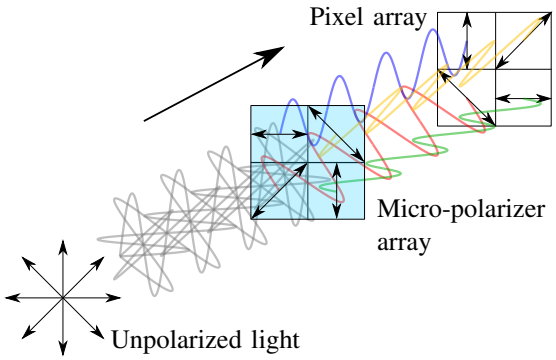

Fig. 1: Arrangement of the wire grid polarizer and pixel arrays.

C. Image pre-processing

1) Irradiance: In this work, an image is a two-dimensional intensity or irradiance array. It is a map I, defined as a compact two-dimensional rectangular region Ω occupied by the image sensor, taking values within the positive real numbers. So, I can be written as the function [42]

$$I : \Omega \subset \mathbb{R}^2 \to \mathbb{R}_+; \quad (x, y) \mapsto I(x, y). \tag{6}$$

For the digital image sensor used in this work, $\Omega = [1, 2056] \times [1, 2464] \subset \mathbb{Z}^2$, and $\mathbb{R}_+$ of the digitized image is an interval of integers $[0, 255] \subset \mathbb{Z}_+$.

2) Convolution: The convolution of a kernel F of size $m \times n$ with an image $I(x, y)$, denoted by $(F * I)(x, y)$ is defined [43] as

$$(F * I)(x, y) = \sum_{s=-a}^{a} \sum_{t=-b}^{b} F(s, t) I(x - s, y - t) \tag{7}$$

where the minus signs align the coordinates of I, and F, when one of the functions is rotated by 180 deg. In this paper, a $*$ symbol is a convolution operator.

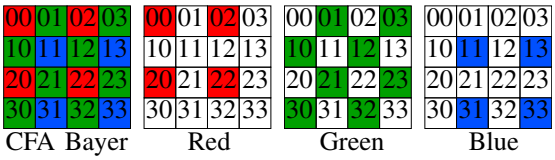

Fig. 2: Color filter array subsampled channels.

3) CFA demosaicing: The value of the missing pixels, for each of the three color subsampled images of a color sensor using a Bayer filter pattern, can be estimated by bilinear interpolation [18]. If a 4×4 pixels area of the sensor and the subsampled red color channel image are taken as an example, as shown in Fig. 2, it can be stated that

$$\begin{aligned} \hat{I}^R(1,1) &= \frac{1}{4}[I^R(0,0) + I^R(2,0) + I^R(0,2) + I^R(2,2)], \\ \hat{I}^R(0,1) &= \frac{1}{2}[I^R(0,0) + I^R(0,2)] \end{aligned} \tag{8}$$

Then, it can be inferred that an estimation of every color channel image can be compactly expressed by convolution as

$$\begin{aligned} \hat{I}^R(x, y) &= (F^{R,B} * I^R)(x, y), \\ \hat{I}^G(x, y) &= (F^G * I^G)(x, y), \\ \hat{I}^B(x, y) &= (F^{R,B} * I^B)(x, y) \end{aligned} \tag{9}$$

with the kernels

$$F^{R,B} = \begin{bmatrix} 1 & 2 & 1 \\ 2 & 4 & 2 \\ 1 & 2 & 1 \end{bmatrix} \cdot \frac{1}{4}, \quad F^G = \begin{bmatrix} 0 & 1 & 0 \\ 1 & 4 & 1 \\ 0 & 1 & 0 \end{bmatrix} \cdot \frac{1}{4} \tag{10}$$

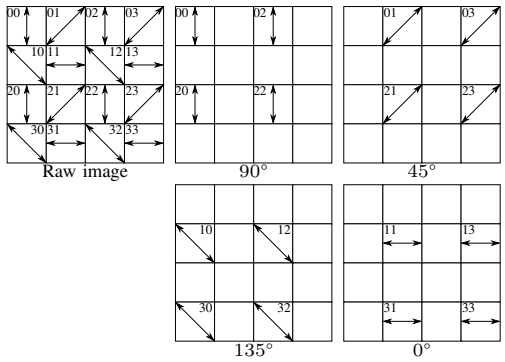

Fig. 3: Micro-polarizer filter array subsampled channels.

4) PFA demosaicing: The value of the missing pixels, for each of the four polarization angle subsampled channel images captured by a DoFP sensor, can be estimated by applying a filter adapted from the pseudo-panchromatic image (PPI) [19].

If a 4×4 pixels area of the DoFP sensor, and the subsampled 90 deg of polarization channel images are taken as an example, as shown in Fig. 3, it can be stated that

$$\begin{aligned}\hat{I}_{90}(1,1) &= \frac{1}{4}[I_{90}(0,0) + I_{90}(2,0) + I_{90}(0,2) + I_{90}(2,2)] \\ \hat{I}_{90}(0,1) &= \frac{1}{2}[I_{90}(0,0) + I_{90}(0,2)]\end{aligned} \tag{11}$$

Then, it can be inferred that the estimation of every polarization channel image can be compactly expressed by convolution as

$$\hat{I}_a(x,y) = (F_{PPI} * I_a)(x,y), \quad a \in \{0, 45, 90, 135\} \tag{12}$$

with the kernel

$$F_{PPI} = \begin{bmatrix} 1 & 2 & 1 \\ 2 & 4 & 2 \\ 1 & 2 & 1 \end{bmatrix} \cdot \frac{1}{16} \tag{13}$$

which is normalized, so that the sum of all its elements is equal to one [44].

D. Image processing

1) Color to grayscale conversion: From the many different methods for converting an RGB image to grayscale [45], in this work, a standard method based on luminance was used [46]. An equivalent grayscale of a color image, can be computed by the weighted combination of its RGB color channels as

$$I^{\text{gray}}(x,y) = 0.3I^R(x,y) + 0.59I^G(x,y) + 0.11I^B(x,y) \tag{14}$$

2) Savitzky-Golay filters: S-G filters are commonly used for smoothing the data captured from a noisy measured signal [47]. In this work, S-G filters are used to compute the smoothed I_s, and first derivative I_d images of the laser, before performing the laser line extraction algorithms. The S-G smoothing F_s, and first derivative F_d filters use the least-squares polynomial approximation [48], and utilizes a simple convolution operation

$$I_s(x,y) = (F_s * I)(x,y), \quad I_d(x,y) = (F_d * I)(x,y) \tag{15}$$

For implementing the S-G smoothing and first derivative filters, the coefficients from [49] were used.

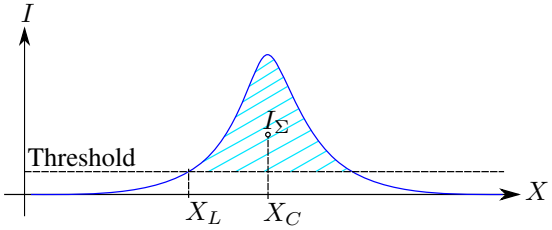

Fig. 4: Center Of Gravity method diagram.

3) Center of gravity method: The COG method is one of the most common methods for extracting the laser line coordinates from an image [50]. It is based on the computation of the COG with subpixel precision by means of the sum of intensities I_Σ, and the sum of the first order moments M_Σ

$$\begin{aligned}X_{C_j} &= X_L + \frac{M_\Sigma}{I_\Sigma} = X_L + \frac{\sum_{i=1}^{N} x_i I(x_i, y_j)}{\sum_{i=1}^{N} I(x_i, y_j)}, \\ Y_{C_j} &= y_j\end{aligned} \tag{16}$$

where N is the number of pixels of the profile, and X_L is the left edge of the laser profile, see Fig. 4.

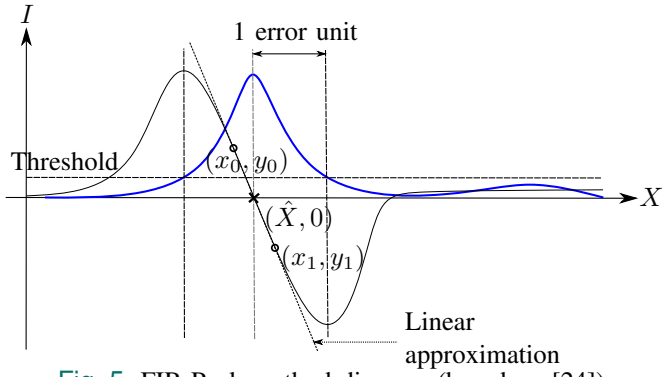

Fig. 5: FIR-Peak method diagram (based on [24]).

4) FIR-Peak method: The main property behind the FIR filter approach [24], is that the first derivative of the convolution of a signal with a filter, is equivalent to the convolution of a signal with the first derivative of the filter

$$I_d(n) = \frac{d}{dn}[I(n) * F(n)] = I(n) * \frac{dF(n)}{dn} = (I * F_d)(n) \tag{17}$$

where $I(n)$ is the laser signal in the row, $F(n)$ is the coefficients of the filter, $I_d(n)$ is the first derivative of the filtered laser signal row, and F_d is the coefficients of the first derivative filter.

The method consists of finding the laser signal maximum value, then finding the first negative value, and compute a line between the last positive (x_0, y_0), and first negative (x_1, y_1) values. This procedure is represented in Fig. 5, and can be summed up in the following expression

$$\hat{X} = x_0 - \frac{y_0 \cdot (x_1 - x_0)}{y_1 - y_0} \tag{18}$$

where $\hat{X}$ is the estimated position of the zero-crossing.

III. Proposed Polarization Vision System

In this work, we propose a polarization vision system, which can be used for scanning, and inspection of surfaces made of highly reflective metals like aluminium. The system includes the data processing pipeline, which goes from the acquisition of the raw polarization image produced by the polarization CIS, to extracting the laser line coordinates with subpixel precision from the optimized polarization image.

The proposed polarization vision system can be implemented using commercial off-the-shelf components: an industrial polarization CIS camera (color or monochrome capable), a generic C-mount lens, a laser line projector, and an

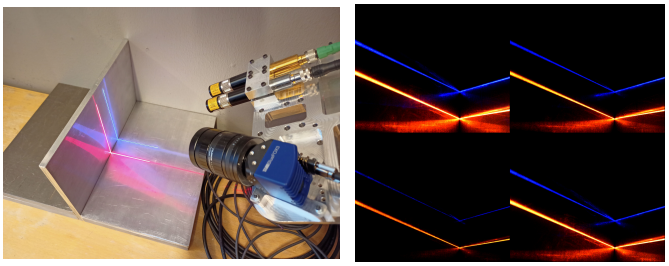

(a) Physical setup for image acquisition. (b) Acquired images for different polarization angles.

Fig. 6: Comparison of the polarization camera images for the red (640 nm), and blue (450 nm) lasers.

embedded platform to compute the algorithms. The CIS is assumed to be a DoFP polarization CIS, which is implemented in a generic industrial camera (i.e., GenICam). Such cameras, often integrate a firmware that usually runs on an embedded FPGA, that takes care of the lower level pre-processing part, such as defective pixels, and dark current corrections, or adjusting the shutter speed. The laser line projector is assumed to be operating in the visible spectrum, and projecting a homogeneous line (i.e., the same light intensity along the line).

In our preliminary tests, when designing the polarized vision system, a red laser operating at 640 nm was used as a reference. As it is broadly used in the industry, and it was previously used in [8]. In order to minimize the noise introduced in the vision system, a blue version of the laser operating at 450 nm was chosen, because of the reduced speckles interference [51], due to its shorter wavelength. Hence, making this laser more suitable for the specific purpose of scanning very reflective metals (e.g., aluminium alloy 6082). An experimental comparison of both lasers revealed that the blue laser displays a smaller amount of reflections for the 4 polarization angle images captured by the CIS, see Fig. 6. In the proposed system we aim to use an affordable machine vision laser line projector. Thus, some optical specifications are not given by the technical datasheets and cannot be used as input to the proposed algorithm (e.g., Stokes vector values).

The polarization vision system imaging methods presented in this work, are divided into three groups, see Fig. 7, depending on the image processing stage: pre-processing, optimization, and processing. In the pre-processing stage, the raw polarization image is demosaiced to a 12 channels color polarization image. In the optimization stage, the 12 channels polarization image is converted to a single-channel image, exploiting the special capabilities of the polarization CIS. In the processing stage, the position of the laser line is extracted with subpixel precision.

The methods were specially developed to be easy to pipeline, so that the output of each stage can become the input for the next stage. As a result, 8 different image processing pipelines can be implemented. Based on the combination of the 2 pre-processing methods, the 2 optimization methods, and the 2 processing methods. All the methods were developed to avoid computational expensive operations whenever possible, by means of using basic operations (e.g., subsampling and convolution), in a way that a pipeline implemented using the proposed methods can run on an embedded system.

IV. Color Polarization Image Pre-Processing

Algorithm 1 Quarter resolution CPFA demosaicing (PolarDemQR)

Input: Polarization image sensor raw image $I_{\text{raw}}(x_{\text{raw}}, y_{\text{raw}})$
Output: 12 channels quarter res. polarization image $\hat{I}_a^c(\frac{x_{\text{raw}}}{2}, \frac{y_{\text{raw}}}{2})$
$a \in \{0, 45, 90, 135\}, \quad c \in \{\text{Red}, \text{Green}, \text{Blue}\}$

procedure PolarDemQR($I_{\text{raw}}(x_{\text{raw}}, y_{\text{raw}})$)
  $x \leftarrow \frac{x_{\text{raw}}}{2}$ ▷ Half of the raw image rows
  $y \leftarrow \frac{y_{\text{raw}}}{2}$ ▷ Half of the raw image columns
  for every pixel **in** x row **do** ▷ Sub and downsampling
    for every pixel **in** y column **do** ▷ from 1 to 4 channels
      $I_{90}(x, y) \leftarrow I_{\text{raw}}(2x, 2y)$
      $I_{45}(x, y) \leftarrow I_{\text{raw}}(2x, 2y + 1)$
      $I_{0}(x, y) \leftarrow I_{\text{raw}}(2x + 1, 2y + 1)$
      $I_{135}(x, y) \leftarrow I_{\text{raw}}(2x + 1, 2y)$
  for every $\{0, 45, 90, 135\}$ **in** a **do** ▷ RGGB subsampling
    for every pixel **in** $x/2$ row **do** ▷ from 4 to 12 channels
      for every pixel **in** $y/2$ column **do**
        $\bar{I}_a^R(2x, 2y) \leftarrow I_a(2x, 2y)$ ▷ Red
        $\bar{I}_a^G(2x + 1, 2y) \leftarrow I_a(2x + 1, 2y)$ ▷ Green
        $\bar{I}_a^G(2x, 2y + 1) \leftarrow I_a(2x, 2y + 1)$ ▷ Green
        $\bar{I}_a^B(2x + 1, 2y + 1) \leftarrow I_a(2x + 1, 2y + 1)$ ▷ Blue
  for Every $\{0, 45, 90, 135\}$ **in** a **do** ▷ Color data est.
    for Every $\{\text{Red}, \text{Green}, \text{Blue}\}$ **in** c **do**
      $\hat{I}_a^c(x, y) \leftarrow F^c(s, t) * \bar{I}_a^c(x, y)$ ▷ Convolution
  return $\hat{I}_a^c(x, y)$ ▷ Output is a 12 channels polarization im.

In this section, we propose two demosaicing methods to reconstruct the 12 channels from a CPFA sensor raw image, which combines both, a CFA, and a PFA, in a single CIS. The methods are developed in a general manner but are specifically adapted to the Sony IMX250MYR sensor (see Section VII-A). The IMX250MYR uses the PFA arrangement in Fig. 3, but it does not follow the standard Bayer pattern in Fig. 2. It uses a Quad Bayer Coding (QBC) [52], for the arrangement of its CFA elements instead. Then, the superpixel array configuration for the raw image, can be obtained by adding the PFA to the QBC arrangement, see Fig. 7.

A. Quarter resolution CPFA demosaicing

The strategy for performing the CPFA demosaicing of the raw image is summarized in Fig. 8. In the first step, 4 subsampled images are created, one for each linear polarization angle (0, 45, 90 and 135 deg). Then, the 4 images are downsampled, reducing both, the vertical, and horizontal resolution by a factor of 2. Resulting in images that are one-quarter of their original resolution. At this point, the PFA demosaicing part of the process is done, as the outcome is 4 lower resolution color images in Bayer pattern. After that, the CFA demosaicing part of the CPFA process starts (similarly as in Section II-C.3), where each of the 4 subsampled and downsampled images are subsampled again. But this time, 3 subsampled images are generated for each of the 4 linear polarization angles, and one for each color channel (red, green and blue), creating a 12

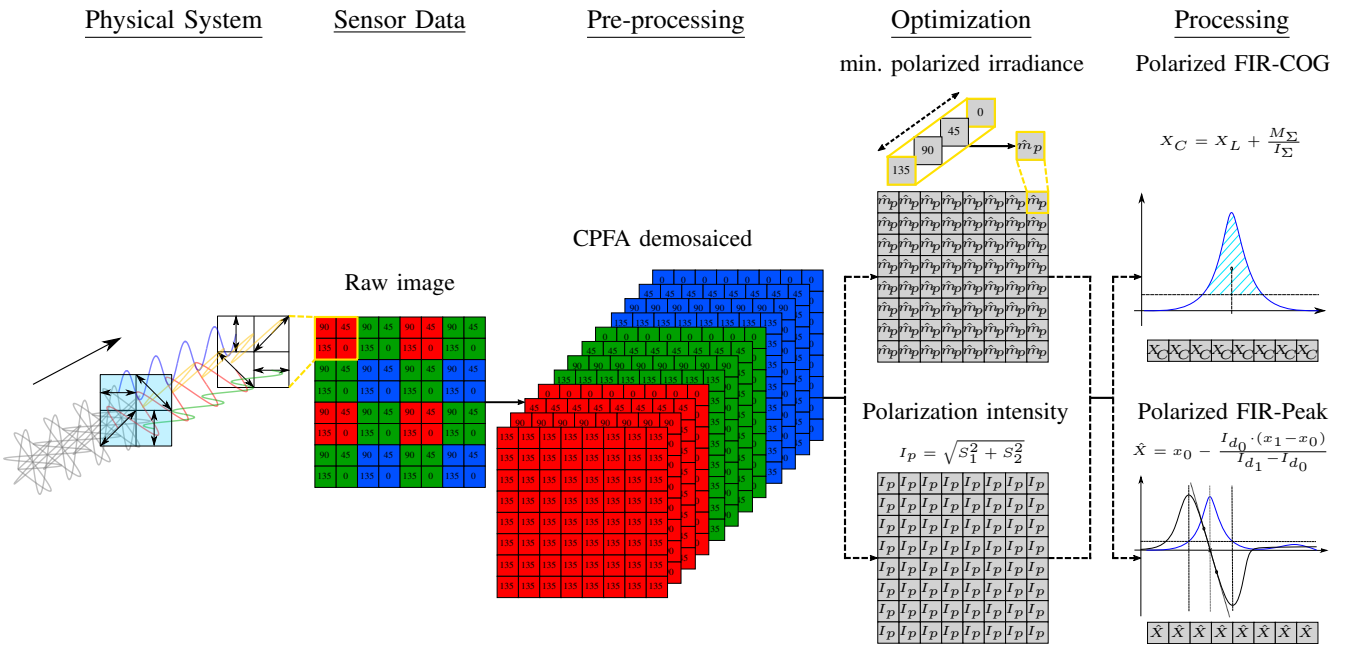

Fig. 7: Overview of the polarization vision system.

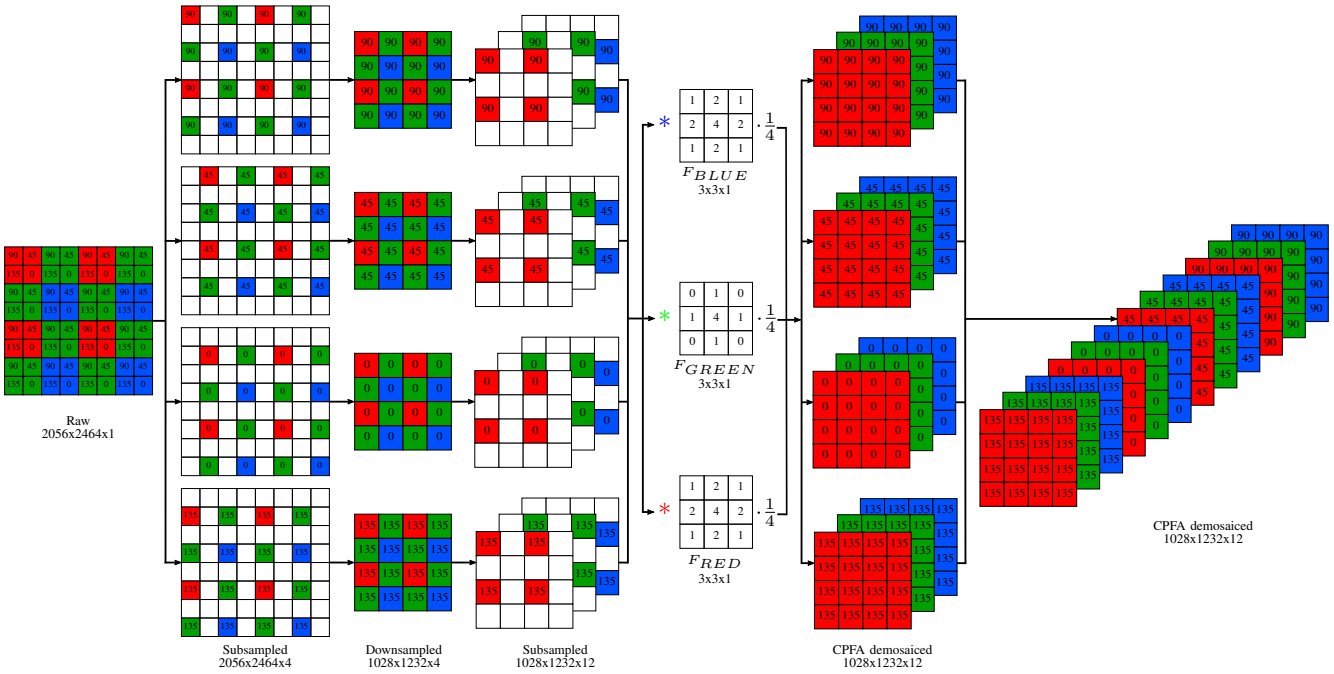

Fig. 8: Quarter resolution CPFA demosaicing.

images array as an outcome. Then, a convolution operation is applied for each of the 12 channels with the corresponding kernel (10), for each color channel. As a result, a 12 channels CPFA demosaiced image, with one-quarter of the original raw image resolution is generated.

B. Full resolution CPFA demosaicing

The one-quarter resolution image results obtained by the procedure shown in Fig. 8, can readily be used in further stages of the pipeline. Although, for the cases where the full original resolution is required, we propose the extension of the method which is summed up in Fig. 9. It is, however, noted that using full-resolution images in further calculations requires more computational power.

The first step consists of performing upsampling, in a way that the 4 different polarizer angles images are combined again in one image. This process is repeated for the 3 different color channels. Then, the 3 color channel images are subsampled, as in Fig. 3. In the final step, the 12 channels are convolved with the pseudo-panchromatic-image kernel (13), to estimate the missing information in each channel. The resulting image is a 12 channels image, in which every channel exhibits the full resolution provided by the polarization CIS.

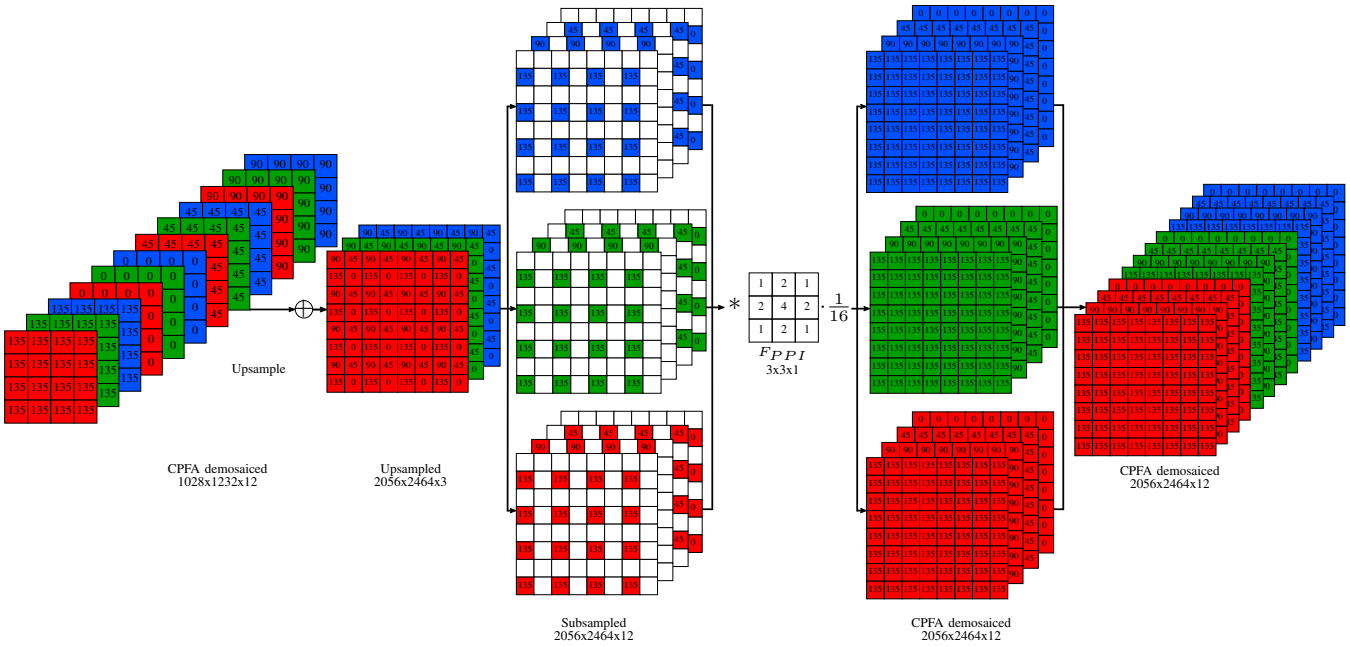

Fig. 9: Full resolution CPFA demosaicing.

Algorithm 2 Full resolution CPFA demosaicing (PolarDemFR)

Input: 12 channels quarter resolution polarization image $\hat{I}_a^c(x,y)$
Output: 12 channels full resolution polarization image $\hat{I}_a^c(2x,2y)$, $a \in \{0,45,90,135\}$, $c \in \{\text{Red},\text{Green},\text{Blue}\}$

procedure PolarDemFR($\hat{I}_a^c(x,y)$)
  for every $\{\text{Red},\text{Green},\text{Blue}\}$ **in** c **do** ▷ Upsampling
    for every pixel **in** x row **do** ▷ from 12 to 4 channels
      for every pixel **in** y column **do**
        $\bar{I}^c(2x,2y) \leftarrow \hat{I}^c_{90}(x,y)$
        $\bar{I}^c(2x,2y+1) \leftarrow \hat{I}^c_{45}(x,y)$
        $\bar{I}^c(2x+1,2y+1) \leftarrow \hat{I}^c_{0}(x,y)$
        $\bar{I}^c(2x+1,2y) \leftarrow \hat{I}^c_{135}(x,y)$
  for every $\{\text{Red},\text{Green},\text{Blue}\}$ **in** c **do** ▷ Subsampling
    for every pixel **in** x row **do** ▷ from 4 to 12 channels
      for every pixel **in** y column **do**
        $\bar{I}^c_{90}(2x,2y) \leftarrow \bar{I}^c(2x,2y)$
        $\bar{I}^c_{45}(2x,2y+1) \leftarrow \bar{I}^c(2x,2y+1)$
        $\bar{I}^c_{0}(2x+1,2y+1) \leftarrow \bar{I}^c(2x+1,2y+1)$
        $\bar{I}^c_{135}(2x+1,2y) \leftarrow \bar{I}^c(2x+1,2y)$
  for every $\{0,45,90,135\}$ **in** a **do** ▷ Polar. channels est.
    for every $\{\text{Red},\text{Green},\text{Blue}\}$ **in** c **do**
      $\hat{I}^c_a(2x,2y) \leftarrow F_{\text{PPI}}(s,t) * \bar{I}^c_a(2x,2y)$ ▷ Convolution
  return $\hat{I}^c_a(2x,2y)$ ▷ Output is a 12 channels polar. im.

V. Color Polarization Image Optimization

In this section, we propose two methods for optimizing images of a polarization CIS, using either irradiance, or polarization. The output of the presented methods will be further processed, using one of the laser line extraction methods presented in Section VI.

New abbreviations for the optimization methods are introduced, as follows: Standard Grayscale Optimization (SGO). Minimum Linearly Polarized Irradiance Optimization (MLPIO) and Polarization Intensity Optimization (PIO).

Algorithm 3 Minimum linearly polarized irradiance image creation (MinLPI)

Input: 12 channels polarization image $I_a^c(x,y)$, $a \in \{0,45,90,135\}$, $c \in \{\text{Red},\text{Green},\text{Blue}\}$
Output: Minimum linearly polarized irradiance image $\hat{m}_p(x,y)$

procedure MinLPI($I_a^c(x,y)$)
  for every $\{0,45,90,135\}$ **in** a **do** ▷ from 12 to 4 channels
    for every pixel **in** x row **do**
      for every pixel **in** y column **do**
        $I_a^{\text{gray}}(x,y) \leftarrow 0.3I_a^R(x,y) + 0.59I_a^G(x,y) + 0.11I_a^B(x,y)$ ▷ Monochrome
  for every $\{0,45,90,135\}$ **in** a **do** ▷ from 4 to 1 channel
    for every pixel **in** x row **do**
      for every pixel **in** y column **do**
        $\hat{m}_p(x,y) \leftarrow \min[I_a^{\text{gray}}(x,y)]$ ▷ Minimum
  return $\hat{m}_p(x,y)$ ▷ Output is a 1 channel image

A. Optimization based on minimum linearly polarized irradiance

This method for optimizing the 12 channels image produced in Section IV, is based on irradiance processing. The method is depicted in Fig. 10, and it assumes a 12 channels image as its input. In the first step, the 12 channels are reduced to 4 channels by computing a monochrome version of the image, which contains the information of the 4 linear polarization angles. Then, the 4 channels are analyzed in a pixel-by-pixel manner, and only the minimum irradiance value $\hat{m}_p$ of each pixel position in every channel is kept. Mathematically, this is described as

$$\hat{m}_p(x,y) = \min[I_a^{\text{gray}}(x,y)], \quad a \in \{0,45,90,135\} \tag{19}$$

As a result, a single-channel optimized image, that represents the minimum linearly polarized irradiance is produced. The method is compactly presented in Algorithm 3.

This article has been accepted for publication in IEEE Sensors Journal. This is the author's version which has not been fully edited and content may change prior to final publication. Citation information: DOI 10.1109/JSEN.2022.3194258

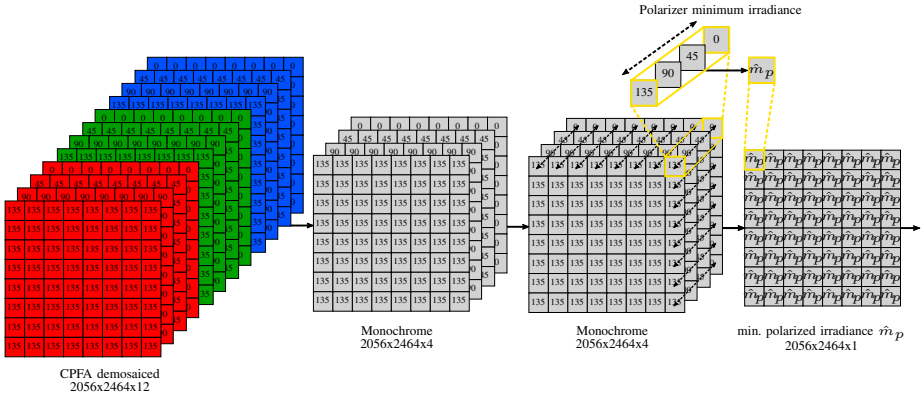

Fig. 10: Polarization image optimization based on the minimum linearly polarized irradiance. Full resolution images are shown, but the procedure is the same for one quarter resolution images.

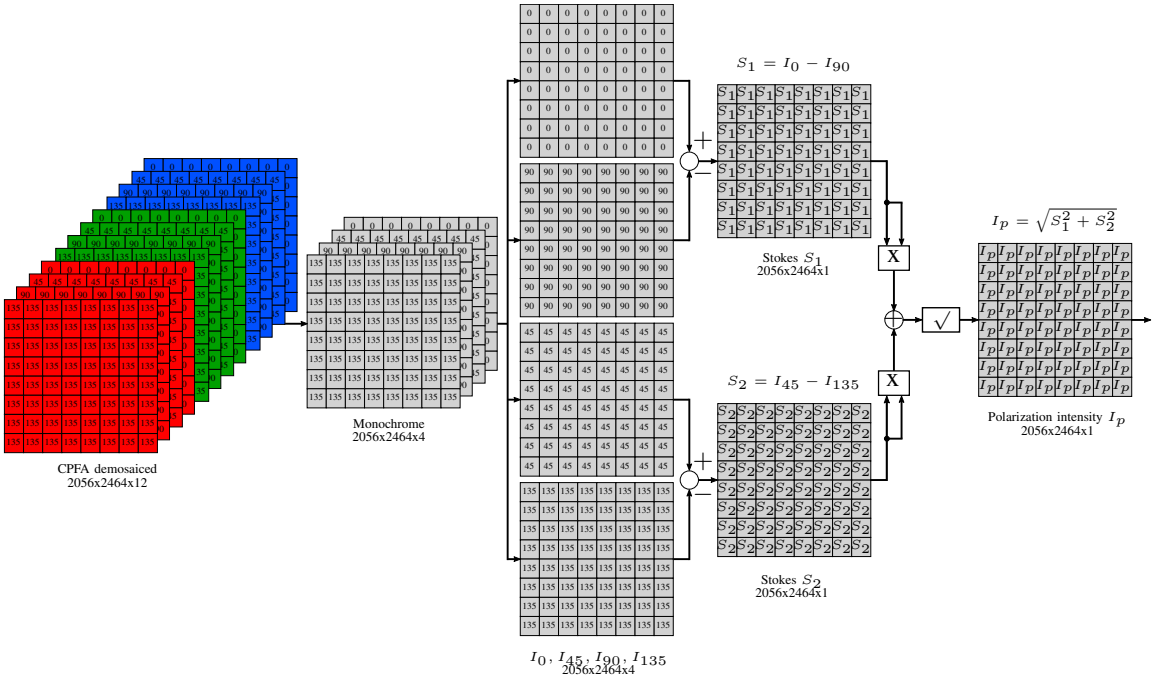

Fig. 11: Polarized image optimization based on the polarization intensity. Full-resolution images are shown, but the procedure is the same for one-quarter resolution images.

B. Optimization based on polarization intensity

In this method, the optimized image is produced based on polarization processing. The initial part of the method, is similar to Section V-A, as we assume a 12 channels image as its input. Then, the 12 channels are reduced to 4 channels, by computing a monochrome version of the image, which contains the information of the 4 linear polarization angles. The rest of the method, is depicted in Fig. 11. As it was described in Section II-B, the state of polarization of the light can be represented using the Stokes parameters (4). The total linear polarization intensity I_{Lpol}, can be computed using the Stokes parameters as

$$I_{\text{Lpol}} = \sqrt{S_1^2 + S_2^2} \tag{20}$$

where the circular component S_3 is removed. Then, (20) can be expanded using (4) as

$$I_{\text{Lpol}} = \sqrt{[(I_0 - I_{90})]^2 + [(I_{45} - I_{135})]^2} \tag{21}$$

Following this procedure, an optimized single-channel image is obtained by means of polarization processing. The method is compactly presented in Algorithm 4.

VI. Polarization Images Laser Line Extraction

In this section, two novel methods for extracting the laser line from the optimized polarization images are presented. Both methods, are based on the output of the optimization stage explained in Section V.

A. Polarized FIR-COG method

In this method, the strategy for computing the coordinates of the laser line in the optimized polarization image is based

Algorithm 4 Polarization Intensity image creation (PolarInt)

Input: 12 channels polarization image $I_a^c(x,y)$, $a \in \{0, 45, 90, 135\}$, $c \in \{\text{Red}, \text{Green}, \text{Blue}\}$
Output: Polarization Intensity image $I_p(x,y)$

procedure POLARINT($I_a^c(x,y)$)
  for every $\{0, 45, 90, 135\}$ **in** a **do** ▷ from 12 to 4 channels
    for every pixel **in** x row **do**
      for every pixel **in** y column **do**
        $I_a^{\text{gray}}(x,y) \leftarrow 0.3I_a^R(x,y) + 0.59I_a^G(x,y) + 0.11I_a^B(x,y)$ ▷ Monochrome
  for every pixel **in** x row **do**
    for every pixel **in** y column **do**
      $S_1(x,y) \leftarrow I_0^{\text{gray}}(x,y) - I_{90}^{\text{gray}}(x,y)$ ▷ Stokes S_1
      $S_2(x,y) \leftarrow I_{45}^{\text{gray}}(x,y) - I_{135}^{\text{gray}}(x,y)$ ▷ Stokes S_2
      $I_p(x,y) \leftarrow \sqrt{S_1(x,y)^2 + S_2(x,y)^2}$ ▷ Polar. Int.
  return $I_p(x,y)$ ▷ Output is a 1 channel image

on the COG explained in Section II-D.3, which is adapted for the polarization vision system. The algorithm, shown in Algorithm 5, is developed for the raw image data coming from the polarization CIS. The raw image is demosaiced using one-quarter resolution, and converted to its full resolution, see Section IV. Then, the demosaiced image undergoes one of the two optimization methods presented in Section V. The resulting image of the chosen optimization method is thresholded, using a constant value via a comparator operation. This thresholded image, is convolved on a column-by-column basis with a 1-dimensional S-G FIR filter kernel for smoothing, see Section II-D.2. Then, every column is analyzed pixel-by-pixel, to detect where the left edge of the laser profile starts. Once the left edge of the laser is found, the part of the column containing the laser signal is processed using the COG algorithm. As a result, the x coordinates of the laser line in the image with sub-pixel precision can be found as

$$X_C = X_L + \frac{M_\Sigma}{I_\Sigma} \tag{22}$$

where X_L is the x coordinate of the left edge pixel, the sum of moments $M_\Sigma = \sum x_i I(x_i, y_j)$, and the sum of intensities $I_\Sigma = \sum I(x_i, y_j)$. The full process of the Polarized FIR-COG method, is depicted in the upper part of Fig. 12.

B. Polarized FIR-Peak method

In this method, the strategy for computing the coordinates of the laser line in the optimized polarization image is based on the FIR-Peak zero-crossing explained in Section II-D.4, which is adapted for the polarization vision system. As previously mentioned, the algorithm, shown in Algorithm 6, is developed for the raw image data coming from the polarization CIS. The pre-processing, optimization, thresholding and smoothing steps are the same as explained in Section VI-A. The smoothed image is then convolved on a column-by-column basis with a 1-dimensional S-G FIR filter kernel for computing the first derivative, see Section II-D.2. Then, every column is analyzed in a pixel-by-pixel manner, to detect the zero-crossing of the differentiated column. Once the zero-crossing is found, the estimated zero-crossing position is computed. As a result, the

Algorithm 5 Polarized FIR-COG method (PolarFIRCOG)

Input: Polarized image sensor raw image $I_{\text{raw}}(x,y)$
Output: Position of the laser line in image coordinates $X_C(1,y)$

procedure POLARFIRCOG($I_{\text{raw}}(x,y)$)
  $\bar{I}_a^c(\frac{x}{2}, \frac{y}{2}) \leftarrow \text{PolarDemQR}(I_{\text{raw}}(x,y))$ ▷ Demos. $^1/_4$ res.
  if Full Resolution demosaicing **then**
    $\hat{I}_a^c(x,y) \leftarrow \text{PolarDemFR}(\bar{I}_a^c(\frac{x}{2}, \frac{y}{2}))$ ▷ Demos. Full res.
  if Minimum linearly polarized irradiance method **then**
    $I_{\text{opt}}(x,y) \leftarrow \text{MinLPI}(\hat{I}_a^c(x,y))$
  else if Polarization Intensity method **then**
    $I_{\text{opt}}(x,y) \leftarrow \text{PolarInt}(\hat{I}_a^c(x,y))$
  for every pixel **in** x row **do**
    for every pixel **in** y column **do**
      if $I_{\text{opt}}(x,y) >$ Threshold **then**
        $I_T(x,y) \leftarrow I_{\text{opt}}(x,y)$ ▷ Thresholded image
  for every j column **in** $I_T(x,y_j)$ **do**
    $I_s(x,1) \leftarrow F_s(k,1) * I_T(x,y_j)$ ▷ S-G smoothing filter
    $X_L \leftarrow 0$ ▷ Initialize left edge of laser profile
    for every i pixel **in** $I_s(x_i,1)$ **do**
      if $X_L = 0$ **and** $I_s(x_i,1) > 0$ **then**
        $X_L \leftarrow x_i$ ▷ Left edge of laser profile
      $I_\Sigma \leftarrow \sum I_s(x_i)$ ▷ Sum of intensities
      $M_\Sigma \leftarrow \sum x_i I_s(x_i)$ ▷ Sum of moments
    $X_C(1,y_j) \leftarrow X_L + \frac{M_\Sigma}{I_\Sigma}$ ▷ COG position of the col.
  return $X_C(1,y)$ ▷ Laser coords. with sub-pixel precision

x coordinates of the laser line in the image, with sub-pixel precision, can be found as

$$\hat{X} = x_i - \frac{I_d(x_i) \cdot (x_{i+1} - x_i)}{I_d(x_{i+1}) - I_d(x_i)} \tag{23}$$

The full process of the Polarized FIR-Peak method, is depicted in the lower part of Fig. 12.

VII. Experimental Study

In this Section, an experimental study on the performance of the proposed methods is evaluated. This is done by comparing the results of the proposed polarized methods, with the results of a standard (i.e., non-polarized) CIS camera. The polarization vision system in this experimental study was implemented using the hardware, and software architecture presented in [8].

A. Setup

The experiments in this study were conducted using the test setup shown in Fig. 13. The setup consists of a semi-circular rack (1), with a track for a sensor trolley (2). The trolley could be placed tangentially to (1), at the given angles towards the horizontal plane. The trolley offered a stepless angle adjustment range of 10 to 90 deg. A sensor bracket (3), was hinged to the sensor trolley, such that an out-of-rack-plane bracket tilt angle could be adjusted. This sensor bracket, offered an angle adjustment range of 0 to $\pm$50 deg, with a 10 deg step angle. A blue laser line projector (4), and a polarization CIS camera (5), were fixed to the bracket (3). The camera angle measured from the laser axis was 28 deg. Two aluminium plates (6), attached to form a right-angle corner, were located approximately in the geometrical rack center. The

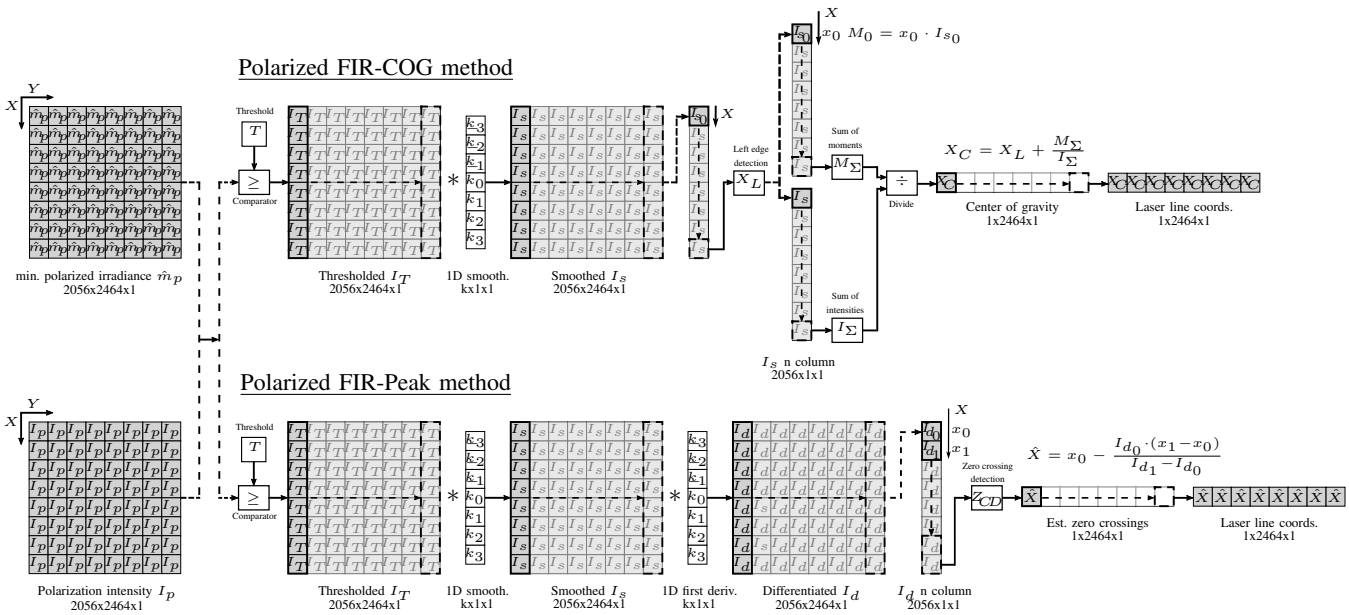

Fig. 12: Polarized FIR-COG and Polarized FIR-Peak methods for laser line extraction from the optimized polarization images.

Algorithm 6 Polarized FIR-Peak method (PolarFIRPeak)

Input: Polarized image sensor raw image $I_{\text{raw}}(x, y)$
Output: Position of the laser line in image coordinates $\hat{X}(1, y)$

procedure PolarFIRPeak($I_{\text{raw}}(x, y)$)
  $\bar{I}_a^c(\frac{x}{2}, \frac{y}{2}) \leftarrow \text{PolarDemQR}(I_{\text{raw}}(x, y))$ ▷ Demos. 1/4 res.
  if Full Resolution demosaicing **then**
    $\hat{I}_a^c(x, y) \leftarrow \text{PolarDemFR}(\bar{I}_a^c(\frac{x}{2}, \frac{y}{2}))$ ▷ Demos. Full res.
  if Minimum linearly polarized irradiance method **then**
    $I_{\text{opt}}(x, y) \leftarrow \text{MinLPI}(\hat{I}_a^c(x, y))$
  else if Polarization Intensity method **then**
    $I_{\text{opt}}(x, y) \leftarrow \text{PolarInt}(\hat{I}_a^c(x, y))$
  for every pixel **in** x row **do**
    for every pixel **in** y column **do**
      if $I_{\text{opt}}(x, y) >$ Threshold **then**
        $I_T(x, y) \leftarrow I_{\text{opt}}(x, y)$ ▷ Thresholded image
  for every j column **in** $I_T(x, y_j)$ **do**
    $I_s(x, 1) \leftarrow F_s(k, 1) * I_T(x, y_j)$ ▷ S-G smoothing filter
    $I_d(x, 1) \leftarrow F_d(k, 1) * I_s(x, 1)$ ▷ S-G first deriv. filter
    for every i pixel **in** $I_d(x_i)$ **do**
      $\bar{X} \leftarrow x_i - \frac{I_d(x_i) \cdot (x_{i+1} - x_i)}{I_d(x_{i+1}) - I_d(x_i)}$ ▷ Zero crossing pred.
    if $\bar{X} > 0$ **then**
      $\hat{X}(1, y_j) \leftarrow \bar{X}$ ▷ Zero crossing est.
  return $\hat{X}(1, y)$ ▷ Laser coords. with sub-pixel precision

trolley, camera, and lateral tilt angles are graphically shown in Fig. 14.

The first camera model used in the tests was a MATRIX VISION mvBlueFOX3-2051pC, which integrates the Sony IMX250MYR 5.07 Megapixels global shutter, and color-capable polarization CIS. The C-Mount FUJINON 1:1.4/16 mm CF16 lens, was mounted on the camera, where the maximum aperture f/1.4 was used in all tests. The laser, was a Z-LASER Z20M18H3-F-450-LP45, outputting 20 mW of power at 450 nm, and projecting a line with a homogeneous distribution of intensity.

For the comparison study, a second, and non-polarized CIS

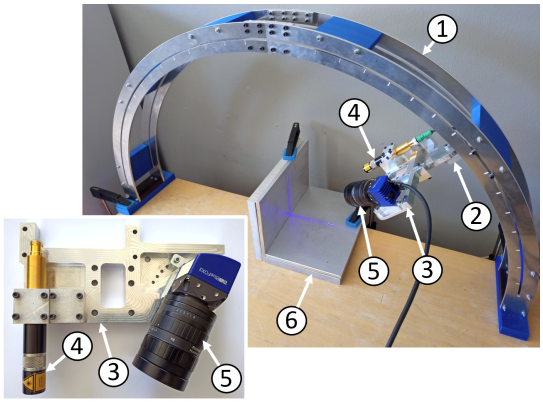

Fig. 13: Test setup: (1) rack, (2) sensor trolley, (3) sensor bracket, (4) blue laser projector, (5) polarization CIS camera and (6) aluminium plates.

was needed. An OMRON STC - MCS500U3V, that integrated a Sony IMX264LLR 5.0 Megapixels global shutter, and color-capable CIS was chosen. The same above-mentioned lens and aperture were used for the OMRON camera tests.

The shutter speed was set manually to 1/30 s, for both cameras. This exposure time configuration was used in all experiments.

The test plates were made of aluminium alloy 6082, which is one of the most common alloys used in industrial aluminium welding [53]. The distance from the laser projector to the AA6082 plates was approximately 300 mm.

The proposed methods were implemented in a C++ application, running on a Real-Time kernel within the Linux4Tegra operating system (OS). This OS was running on an Nvidia Jetson AGX Xavier kit. For more details on the hardware and communication setup, the reader is referred to [8].

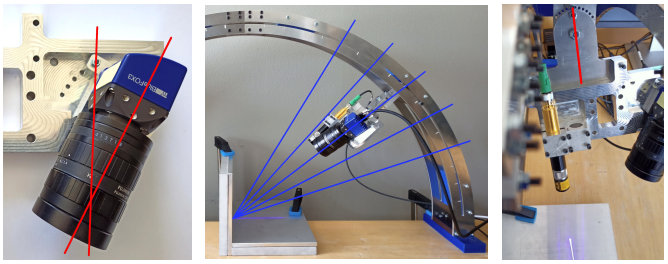

(a) (b) (c)

Fig. 14: Polarization CIS camera angle (a), trolley angle (b), and lateral tilt angle (c).

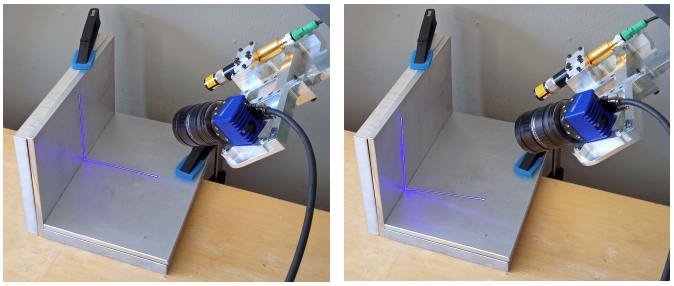

(a) Acquisition, 0 deg lateral tilt. (b) Acquisition, 10 deg lateral tilt.

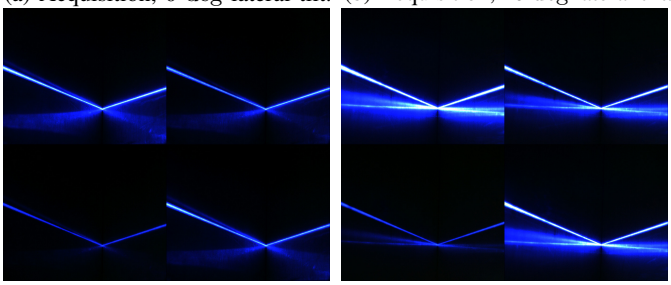

(c) Polarization image, 0 deg lateral tilt. (d) Polarization image, 10 deg lateral tilt.

Fig. 15: Acquisition, and resulting polarization image. A lateral tilt leads to a skewed laser projection, increasing the noise.

B. Methodology and test program

The performance of the proposed methods was studied for two different CIS technologies, different sensor bracket orientations, and under different illumination conditions. Three different trolley angles were considered: 25, 35, and 45 deg. For each trolley angle, two different lateral tilt angles were considered: 0, and 10 deg. A small tilt angle was selected as it is feasible in practical applications when it is desired to scan as close as possible to a 0 deg tilt angle. This way the scanned geometry is represented correctly, while large tilt angles rather "stretch" the nominal geometry in the scan data. Furthermore, the lateral tilt angle of 10 deg was chosen because the tilted laser projector causes interreflections to appear on the aluminium plates. These interreflections produce noise (unwanted variations) in the laser images, see Fig. 15. In addition, two different illumination conditions were used for each orientation: a standard ambient light with a measured illuminance value of approximately 400 lux, and a strong ambient light with a measured illuminance value of approximately 1300 lux. Then, and for each of the mentioned conditions, the following data processing steps were done:

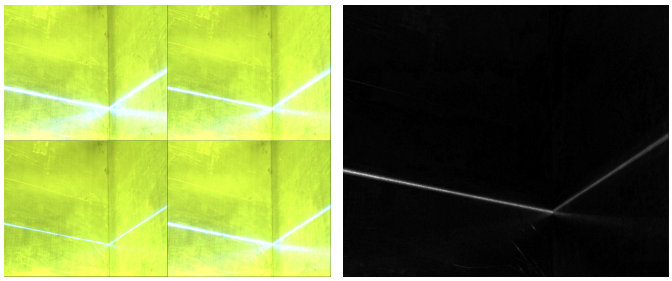

(a) Before optimization. (b) PIO, I_p optimized image.

Fig. 16: Polarization image with strong ambient light example.

1) The Raw image in Fig. 17a, is captured:
2) The different color polarization angle I_0, I_{45}, I_{90} and I_{135} images in Figures 17b, 17c, 17d, and 17e, were pre-processed by means of the full resolution CPFA demosaicing method explained in Section IV;
3) The MLPIO image $\hat{m}_p$ in Fig. 17l, was computed by means of the method explained in Section V-A;
4) The Stokes parameter S_0, S_1, and S_2 images in Figures 17f, 17g and 17h, were computed by means of the equations in 4;
5) The PIO image I_p in Fig. 17k, was computed by means of the method explained in Section V-B;
6) The Polarized FIR-COG images of MLPIO in Fig. 17o, and PIO in Fig. 17m, were computed by means of the method explained in Section VI-A;
7) The Polarized FIR-Peak images of MLPIO in Fig. 17p, and PIO in Fig. 17n, were computed by means of the method explained in Section VI-B.

For the test runs where the standard (non-polarized) camera was used, the data processing was done as close as possible to the previously mentioned steps. The following was altered:

- The standard CFA demosaicing explained in Section II-C.3, was performed in the pre-processing part, since a standard CIS does not implement a PFA;
- The RGB images were converted to a grayscale equivalent, as explained in Section II-D.1, in the optimization part. Since the image does not contain any polarization information.

More intermediate processing results are presented in Fig. 17, providing the reader with a comprehensive view of the data processing steps.

TABLE I: S-G FIR filter kernels (one-dimensional, 7 points and cubic) used for the laser line extraction

Point k	**−3**	**−2**	**−1**	**0**	**1**	**2**	**3**	**norm**
Smoothing	−2	3	6	7	6	3	−2	21
1st deriv.	22	−67	−58	0	58	67	−22	252

Regarding the laser line extraction methods shown in Fig. 12, the global threshold was adjusted manually during the execution of the program to a suitable value and applied to the whole image. Meanwhile, the S-G FIR filter kernels for

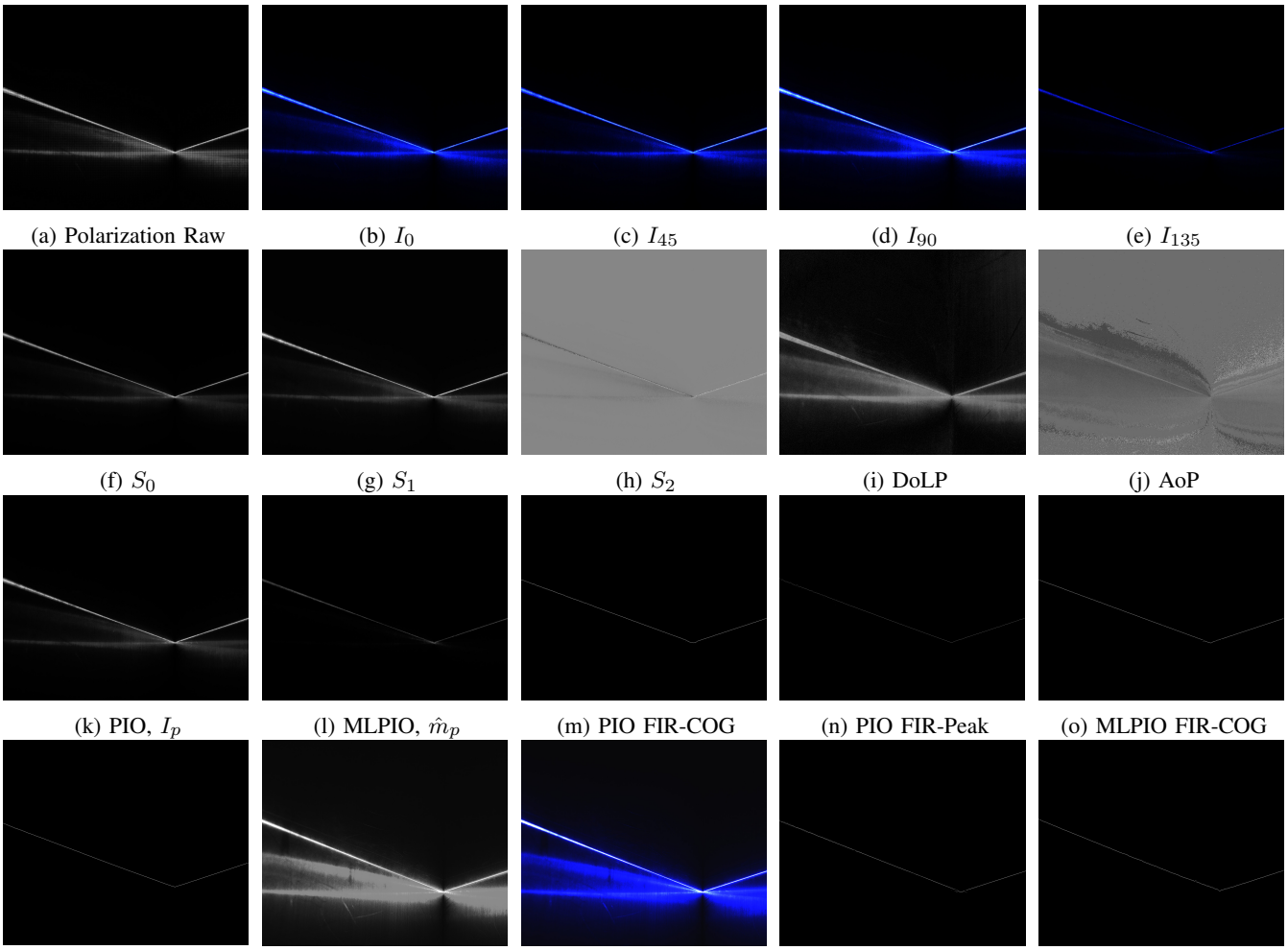

(a) Polarization Raw (b) I_0 (c) I_{45} (d) I_{90} (e) I_{135}

(f) S_0 (g) S_1 (h) S_2 (i) DoLP (j) AoP

(k) PIO, I_p (l) MLPIO, $\hat{m}_p$ (m) PIO FIR-COG (n) PIO FIR-Peak (o) MLPIO FIR-COG

(p) MLPIO FIR-Peak (q) Standard Raw (r) Standard Color (s) SGO FIR-COG (t) SGO FIR-Peak

Fig. 17: Visualization of the image results of different data processing steps.

smoothing and first derivative, explained in Section II-D.2, used for all the experiments, are shown in Table I. These kernels were chosen empirically from [49], for the specific lens, and laser thickness used in our setup.

Once all the data needed was acquired, a method and program for post-processing the data acquired by both, the polarization, and standard cameras had to be devised. In such a way, that the results of both CIS could be compared.

The synthetic (i.e., ground truth) laser line coordinates, were computed by carefully choosing 3 points in every image manually, and doing piecewise linear interpolation between the points afterwards. Due to the arrangement of the test plates in Fig. 13, the shape of the laser in the image was known to have a V-shape. Then, the 3 points were selected at the beginning, corner, and ending of the laser line.

Both CIS have a resolution of approximately 5 Megapixels. The polarization CIS of the MATRIX VISION camera has an image size of $[2056 \times 2464]$ pixels, whereas the CIS of the Omron camera has an image size of $[2048 \times 2448]$ pixels. In order to do a pixel-wise comparison between the CIS, 8 rows, and 16 columns were cropped from the polarization CIS images.

C. Results

The performance of the methods was evaluated and compared in terms of the Mean Absolute Error (MAE) in pixels, and the Peak signal-to-noise ratio (PSNR) in dB, both relative to the synthetic laser. Since these error metrics are widely used in the literature, the reader is referred to [54] for the MAE, and to [55] for the PSNR calculation formulas. To improve the reliability of the results, the processing steps given in Section VII-B were repeated for 10 different sets of images. The averaged MAE and PSNR results over 10 sets of images for all test cases are conveniently collected in Tables II and III.

For the standard ambient light test cases, the results from Table II can be summed up as follows.

On the one hand, for the 0 deg tilt angle over all the trolley angles, the error and PSNR for the polarization CIS were in the range of 0.54-3.58 pixels and 48.66-36.85 dB. Whereas, for the standard CIS the error and PSNR were in the range of 1.20-4.48 pixels, and 43.90-35.12 dB. It is noted that the polarization CIS performed marginally better for all trolley angle test cases. The minimum error and maximum PSNR were achieved using the FIR-COG laser extraction method for all trolley angles tested. For the polarization CIS, the MLPIO

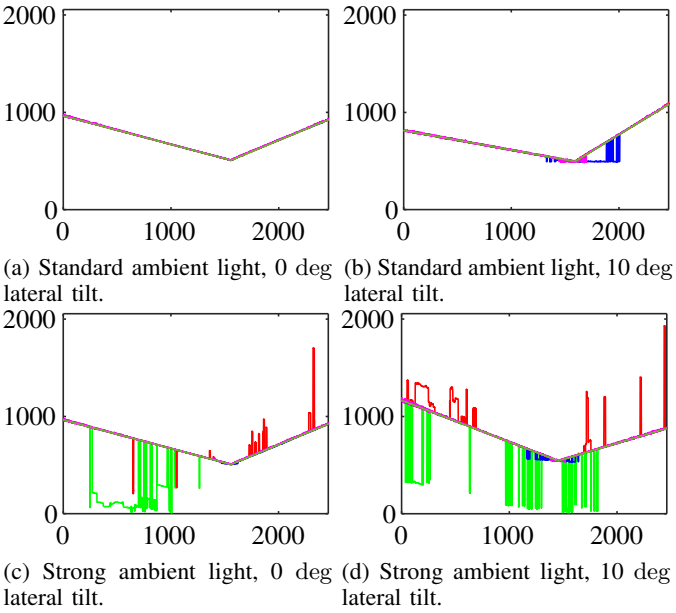

(a) Standard ambient light, 0 deg lateral tilt.

(b) Standard ambient light, 10 deg lateral tilt.

(c) Strong ambient light, 0 deg lateral tilt.

(d) Strong ambient light, 10 deg lateral tilt.

Fig. 18: Laser line coordinates with different noise sources (vertical axis inverted for displaying purposes). Color code for the Synthetic laser and the proposed methods: MLPIO FIR-COG, MLPIO FIR-Peak, PIO FIR-COG, PIO FIR-Peak.

performed better than the PIO for all trolley angles tested. The MAE and PSNR results suggested that both, standard, and polarization CIS, perform well under given conditions.

On the other hand, for the 10 deg tilt angle over all the trolley angles, the results were quite different. The error, and PSNR for the polarization CIS, were in the range of 1.22-12.55 pixels, and 43.49-17.04 dB. Whereas, for the standard CIS, the error, and PSNR were in the range of 1.85-7.42 pixels, and 36.94-22.20 dB. In these test cases, where the 10 deg tilt angle was present, the polarization CIS performed better than the standard CIS for all trolley angles tested. For the polarization CIS, the MLPIO combined with the FIR-Peak performed better than all other optimization and laser extraction methods. The results showed a clear advantage of using the polarization CIS under given conditions.

For the strong ambient light test cases, the results from Table III can be summed up as follows.

On the one hand, for the 0 deg tilt angle over all the trolley angles, the error, and PSNR for the polarization CIS were in the range of 1.36-6.38 pixels, and 39.80-14.37 dB using the PIO. Meanwhile, using the MLPIO, were in the range of 65.23-149.90 pixels, and 3.45-(-1.8) dB. For the standard CIS, the error, and PSNR were in the range of 52.96-566.84 pixels, and 3.44-(-9.6) dB. Besides, the minimum error, and maximum PSNR for the polarization CIS, were achieved using the FIR-COG laser extraction method. These MAE and PSNR results also showed a clear advantage of using the polarization CIS under given conditions.

On the other hand, for the 10 deg tilt angle over all the trolley angles, the error, and PSNR for the polarization CIS were in the range of 3.51-18.87 pixels and 28.24-12.36 dB using the PIO. Meanwhile, using the MLPIO were in the range of 45.68-187.46 pixels, and 5.09-(-3.1) dB. For the standard CIS, the error, and PSNR were in the range of 149.48-303.51 pixels, and (-1.2)-(-5.7) dB. In contradiction with the results for the 0 deg tilt angle, this time the FIR-Peak laser extraction method performed better than the FIR-COG method. The MAE and PSNR results once again showed a clear advantage of using the polarization CIS under given conditions.

Different areas of the laser line image could be affected by the noise present in the measurements, depending on the noise source. Either a big area of the image because of the strong ambient light, or a more localized area of the image in the vicinity of the laser line, because of the interreflections caused by the lateral tilt. An example of incorrect estimation of the laser line coordinates (i.e., large MAE), due to the mentioned noise affecting the laser line extraction, is given in Fig. 18.

D. Discussion

This section contains the discussion of the results given in Section VII-C, and the outcome of our experimental study.

Performance of all methods for the test cases under standard ambient light with 0 deg lateral tilt, is considered acceptable. Whereas, the MLPIO FIR-COG and SGO FIR-COG methods only marginally outperform all the others. It was expected that all methods (even with the standard CIS) would perform well in these test cases, see Fig. 18a. The absence of a lateral tilt reduces the noise in the area of the image in the vicinity of the laser line, and the standard ambient light facilitates achieving a high PSNR laser image. The higher accuracy of the MLPIO method can be attributed to its better ability to filter the diffuse reflections, see Fig. 17l. Which can be considered the dominant noise source for the test cases under standard ambient light with no lateral tilt. It is notable that, for the 10 deg tilt test cases, MLPIO is still the preferred optimization method for the polarization CIS, but in combination with FIR-Peak laser line extraction. Regarding the 10 deg tilt test cases, see Fig. 18b. In addition to the mentioned diffuse reflections, interreflections are caused by the lateral tilt, affecting the area of the image in the vicinity of the laser line, see Fig. 15. These interreflections create their own diffuse reflections, which can be filtered by means of using the MLPIO, see Fig. 15d, which is why it performs better than the standard, and PIO methods. Although the MLPIO cannot filter the noise produced by the interreflection itself, the FIR-Peak method manages to filter this noise more efficiently than FIR-COG, and that is why the MLPIO in combination with FIR-Peak outperforms the other methods in the 10 deg tilt test cases.

Regarding the test cases under strong ambient light conditions, the PIO method provided far better performance, when compared to the SGO and MLPIO methods. In these test cases, the irradiance value of the laser is comparable to the noise caused by the strong ambient light. Hence, the SGO, and MLPIO methods achieve a low PSNR laser image. Providing an unacceptable performance, as they are based on irradiance, and the strong ambient light becomes an interfering input. The MAE difference is large, resulting in that only the PIO method can be recommended under strong ambient light conditions, where unpredictable reflections appear across

TABLE II: MAE in pixels (PSNR in dB inside parentheses) with standard ambient light. The best result is highlighted in red.

	Methods		0 deg lateral tilt			10 deg lateral tilt		
Sensor	Optimization	Laser Ext.	25	35	45	25	35	45
Std. CIS	Std. grayscale (SGO)	FIR-COG	1.20 (43.90)	1.50 (40.96)	1.34 (42.83)	7.42 (22.20)	6.57 (22.77)	4.89 (26.85)
		FIR-Peak	2.56 (37.83)	4.48 (35.12)	4.24 (36.14)	4.00 (27.56)	3.03 (31.30)	1.85 (36.94)
Polar. CIS	Min. linearly polar. irradiance (MLPIO)	FIR-COG	0.86 (47.37)	0.74 (48.06)	0.54 (48.66)	2.73 (34.26)	2.08 (32.86)	1.84 (38.66)
		FIR-Peak	1.78 (42.25)	1.22 (44.60)	1.26 (42.42)	1.27 (42.39)	1.22 (43.49)	1.25 (43.36)
	Polarization intensity (PIO)	FIR-COG	1.54 (44.82)	1.65 (43.88)	1.85 (39.80)	12.55 (17.04)	8.05 (19.22)	6.91 (20.41)
		FIR-Peak	2.96 (39.07)	2.86 (39.66)	3.58 (36.85)	3.59 (26.87)	3.14 (35.90)	2.89 (35.72)

TABLE III: MAE in pixels (PSNR in dB inside parentheses) with strong ambient light. The best result is highlighted in red.

	Methods		0 deg lateral tilt			10 deg lateral tilt		
Sensor	Optimization	Laser Ext.	25	35	45	25	35	45
Std. CIS	Std. grayscale (SGO)	FIR-COG	123.61 (-0.1)	566.84 (-9.6)	438.95 (-7.1)	241.7 (-4.2)	303.51 (-5.7)	286.21 (-3.9)
		FIR-Peak	52.96 (3.44)	374.86 (-6.8)	299.58 (-4.5)	170.84 (-2.2)	149.48 (-1.6)	170.56 (-1.2)
Polar. CIS	Min. linearly polar. irradiance (MLPIO)	FIR-COG	149.90 (-1.8)	82.27 (2.04)	67.19 (3.45)	179.16 (-2.7)	187.46 (-3.1)	54.02 (5.09)
		FIR-Peak	125.32 (0.36)	75.70 (1.62)	65.23 (2.86)	135.78 (0.10)	163.91 (-1.3)	45.68 (4.01)
	Polarization intensity (PIO)	FIR-COG	1.36 (39.80)	1.72 (23.7)	2.35 (25.34)	13.25 (16.12)	18.87 (12.36)	17.75 (14.14)
		FIR-Peak	3.01 (32.17)	6.28 (14.40)	6.38 (14.37)	3.51 (28.24)	6.17 (16.36)	6.93 (14.35)

the surface of the aluminium plates, see Fig. 16a. The better performance can be attributed to the ability of the PIO method to efficiently filter the non-polarized ambient light noise, which can be considered the dominant noise source under the strong ambient light conditions, see Fig. 16. As in the previous 10 deg tilt test cases, the FIR-Peak method manages to filter the interreflections noise more efficiently than FIR-COG.

An interesting result is that the PIO method performs almost identically for both, standard, and ambient light conditions. This robust filtering of the non-polarized light is not only practical under strong ambient light scenarios. But also in the cases where the PSNR of the laser image captured by the CIS is low, because of one or a combination of the following circumstances: strong ambient light, too long exposure time, incorrect or lack of aperture control or the laser power outputted by the projector is too low. This filtering is done by exploiting the polarization capabilities of the color polarization CIS, without any optical narrow bandpass filters, hence leaving the color capabilities of the CIS available.

The PIO method proved to be robust under all test conditions, delivering acceptable results. Besides, the MLPIO method is more accurate because of its ability to filter the diffuse component of the reflections and interreflections, when the PSNR of the laser image captured by the CIS is high but delivers unacceptable results when it is low. Meanwhile, the reason behind the slightly worse accuracy of the PIO method, when compared with the MLPIO method, is that it cannot filter the diffuse reflections as effectively as the MLPIO method can, despite its robustness.

Regarding the performance of the not-fully optimized C++ software running on the Nvidia Jetson. The framerate for a full pipeline implementation, from acquisition to laser line coordinates, was 10-15 FPS for quarter resolution, and 2-4 FPS for full resolution demosaicing. Depending on the optimization, and laser line extraction method chosen.

Based on the results under the given conditions, and discussion. The preferred methods are summarized in Table IV. The experimental results support the scope of this paper where we consider a realistic industrial application when scanning has to be done at 0 deg tilt to maintain the precision of the scanned data. However, small deviations from 0 deg tilt can occur, especially when scanning complex geometries. Therefore, tilt angles up to 10 deg are reasonable to take into consideration in the implementation of an industrial scanning operation. In that perspective, Table IV gives an overview of suggested methods for realistic industrial applications.

TABLE IV: Preferred methods under given conditions.

Ambient Light	0 deg lateral tilt (No interreflections noise)	10 deg lateral tilt (Interreflections noise)
Standard (High PSNR)	MLPIO FIR-COG	MLPIO FIR-Peak
Strong (Low PSNR)	PIO FIR-COG	PIO FIR-Peak

VIII. Conclusions

In this paper, a novel polarization vision system, and its pipeline were presented. In addition, two methods for demosaicing, two methods for optimisation and two methods for laser line extraction, were developed for a polarization CIS. The CPFA demosaicing methods could output either one quarter or full resolution 12 channel images, avoiding computational expensive operations. The proposed irradiance-based MLPIO method was able to efficiently filter the diffuse component of the reflections of the laser. Meanwhile, the proposed polarization-based PIO method is a completely novel approach. This method, facilitates the development of a laser line scanner system based purely on polarization, which is an advantage for the application cases where capturing a high PSNR laser image with a CIS is not possible (i.e. strong ambient light or weak laser), and/or the color capability of the CIS is desired (i.e. no bandpass filter is used). And finally, the Polarized FIR-COG and Polarized FIR-Peak were the proposed methods to extract the laser line coordinates from the optimized polarization images with subpixel precision.

The proposed system was tested by scanning a blue laser line projected onto two aluminium alloy 6082 plates, under two different light conditions, and in six different orientations. The test results suggested that the performance of the

polarization CIS is better compared to the non-polarized CIS, although similar in the less challenging test case where no interreflections are present and the PSNR of the laser image is high. In terms of the optimization methods, the MLPIO method performed better under standard ambient light conditions (PSNR of the laser image is high), due to its ability to efficiently filter the diffuse reflections noise. Whereas, the PIO method performed better under strong ambient light conditions (PSNR of the laser image of the other methods is low), due to its ability to efficiently filter the non-polarized ambient light noise. In terms of the laser line extraction methods, the Polarized FIR-COG performed better, when no interreflections noise was present. Whereas, the Polarized FIR-Peak performed better when the interreflections noise was present.

From an industrial perspective, the presented work can be used as the foundation for designing a pipeline running on the low-level firmware of an industrial laser triangulation system based on polarization sensing.

REFERENCES

[1] C. Steger, M. Ulrich, and C. Wiedemann, *Machine vision algorithms and applications*, 2nd ed. John Wiley & Sons, 2018, pp. 1–3.

[2] S. Soloman, *Sensors and control systems in manufacturing*, 2nd ed. McGraw-Hill Education, 2010, pp. 119–132.

[3] A. Donges and R. Noll, *Laser measurement technology*. Springer, 2016.

[4] M. Gupta, A. Agrawal, A. Veeraraghavan, and S. G. Narasimhan, "A practical approach to 3d scanning in the presence of interreflections, subsurface scattering and defocus," *Int J Comput Vis*, vol. 102, no. 1, pp. 33–55, 2013.

[5] A. Cibicik, L. Tingelstad, and O. Egeland, "Laser scanning and parametrization of weld grooves with reflective surfaces," *Sensors*, vol. 21, no. 14, p. 4791, 2021.

[6] X. Li, X. Li, M. O. Khyam, and S. S. Ge, "Robust welding seam tracking and recognition," *IEEE Sensors J.*, vol. 17, no. 17, pp. 5609–5617, 2017.

[7] J. Fan, F. Jing, L. Yang, L. Teng, and M. Tan, "A precise initial weld point guiding method of micro-gap weld based on structured light vision sensor," *IEEE Sensors J.*, vol. 19, no. 1, pp. 322–331, 2018.

[8] J. Marco-Rider, L. Tingelstad, and O. Egeland, "Polarization image sensor-based laser scanner for reflective metals: architecture and implementation," in *2021 IEEE Sensors*, 2021, pp. 1–4.

[9] J. Ohta, *Smart CMOS image sensors and applications*, 2nd ed. CRC press, 2020, pp. 1–10.

[10] S. Manda, R. Matsumoto, S. Saito, S. Maruyama, H. Minari, T. Hirano, T. Takachi, N. Fujii, Y. Yamamoto, Y. Zaizen *et al.*, "High-definition visible-swir ingaas image sensor using cu-cu bonding of iii-v to silicon wafer." in *2019 IEEE International Electron Devices Meeting (IEDM)*. IEEE, 2019, pp. 16–7.

[11] T. Okino, S. Yamahira, S. Yamada, Y. Hirose, A. Odagawa, Y. Kato, and T. Tanaka, "A real-time ultraviolet radiation imaging system using an organic photoconductive image sensor," *Sensors*, vol. 18, no. 1, p. 314, 2018.

[12] Y. Oike, "Evolution of image sensor architectures with stacked device technologies," *IEEE Trans. Electron Devices*, 2021.

[13] Y. Maruyama, T. Terada, T. Yamazaki, Y. Uesaka, M. Nakamura, Y. Matoba, K. Komori, Y. Ohba, S. Arakawa, Y. Hirasawa *et al.*, "3.2-mp back-illuminated polarization image sensor with four-directional air-gap wire grid and 2.5-um pixels," *IEEE Trans. Electron Devices*, vol. 65, no. 6, pp. 2544–2551, 2018.

[14] R. Walraven, "Polarization imagery," in *Optical Polarimetry: Instrumentation and Applications*, vol. 112. SPIE, 1977, pp. 164–167.

[15] J. S. Tyo, D. L. Goldstein, D. B. Chenault, and J. A. Shaw, "Review of passive imaging polarimetry for remote sensing applications," *Applied optics*, vol. 45, no. 22, pp. 5453–5469, 2006.

[16] J. Hao, Y. Zhao, W. Liu, S. G. Kong, and G. Liu, "A micro-polarizer array configuration design method for division of focal plane imaging polarimeter," *IEEE Sensors J.*, vol. 21, no. 3, pp. 2828–2838, 2020.

[17] A. Abubakar, X. Zhao, S. Li, M. Takruri, E. Bastaki, and A. Bermak, "A block-matching and 3-d filtering algorithm for gaussian noise in dofp polarization images," *IEEE Sensors J.*, vol. 18, no. 18, pp. 7429–7435, 2018.

[18] D. Alleysson, S. Susstrunk, and J. Hérault, "Linear demosaicing inspired by the human visual system," *IEEE Transactions on Image Processing*, vol. 14, no. 4, pp. 439–449, 2005.

[19] S. Mihoubi, P.-J. Lapray, and L. Bigué, "Survey of demosaicking methods for polarization filter array images," *Sensors*, vol. 18, no. 11, p. 3688, 2018.

[20] M. Morimatsu, Y. Monno, M. Tanaka, and M. Okutomi, "Monochrome and color polarization demosaicking based on intensity-guided residual interpolation," *IEEE Sensors J.*, vol. 21, no. 23, pp. 26 985–26 996, 2021.

[21] A. Ahmed, X. Zhao, J. Chang, H. Ma, V. Gruev, and A. Bermak, "Four-directional adaptive residual interpolation technique for dofp polarimeters with different micro-polarizer patterns," *IEEE Sensors J.*, vol. 18, no. 19, pp. 7990–7997, 2018.

[22] R. Fisher and D. Naidu, "A comparison of algorithms for subpixel peak detection," in *Image technology*. Springer, 1996, pp. 385–404.

[23] C. Steger, "Unbiased extraction of lines with parabolic and gaussian profiles," *Computer Vision and Image Understanding*, vol. 117, no. 2, pp. 97–112, 2013.

[24] J. Forest, J. Salvi, E. Cabruja, and C. Pous, "Laser stripe peak detector for 3d scanners. a fir filter approach," in *Proceedings of the 17th International Conference on Pattern Recognition, 2004. ICPR 2004.*, vol. 3. IEEE, 2004, pp. 646–649.

[25] M. Wan, S. Wang, H. Zhao, H. Jia, and L. Yu, "Robust and accurate sub-pixel extraction method of laser stripes in complex circumstances," *Applied Optics*, vol. 60, no. 36, pp. 11 196–11 204, 2021.

[26] X. Xu, Z. Fei, J. Yang, Z. Tan, and M. Luo, "Line structured light calibration method and centerline extraction: A review," *Results in Physics*, vol. 19, p. 103637, 2020.

[27] D. Palousek, M. Omasta, D. Koutny, J. Bednar, T. Koutecky, and F. Dokoupil, "Effect of matte coating on 3d optical measurement accuracy," *Optical Materials*, vol. 40, pp. 1–9, 2015.

[28] T. Kouteckỳ, D. Paloušek, and J. Brandejs, "Sensor planning system for fringe projection scanning of sheet metal parts," *Measurement*, vol. 94, pp. 60–70, 2016.

[29] A. Cibicik, E. B. Njaastad, L. Tingelstad, and O. Egeland, "Robotic weld groove scanning for large tubular t-joints using a line laser sensor," *Int. J. Adv. Manuf. Technol.*, 2022.

[30] D. Scharstein, H. Hirschmüller, Y. Kitajima, G. Krathwohl, N. Nešić, X. Wang, and P. Westling, "High-resolution stereo datasets with subpixel-accurate ground truth," in *German conference on pattern recognition*. Springer, 2014, pp. 31–42.

[31] H. Zhao, Y. Xu, H. Jiang, and X. Li, "3d shape measurement in the presence of strong interreflections by epipolar imaging and regional fringe projection," *Opt. exp.*, vol. 26, no. 6, pp. 7117–7131, 2018.

[32] J. Clark, E. Trucco, and L. B. Wolff, "Using light polarization in laser scanning," *Image and Vision Computing*, vol. 15, no. 2, pp. 107–117, 1997.

[33] Y. Zhongdong, W. Peng, L. Xiaohui, and S. Changku, "3d laser scanner system using high dynamic range imaging," *Optics and Lasers in Engineering*, vol. 54, pp. 31–41, 2014.

[34] A. Kadambi, R. Whyte, A. Bhandari, L. Streeter, C. Barsi, A. Dorrington, and R. Raskar, "Coded time of flight cameras: sparse deconvolution to address multipath interference and recover time profiles," *ACM Transactions on Graphics (ToG)*, vol. 32, no. 6, pp. 1–10, 2013.

[35] N. Matsuda, O. Cossairt, and M. Gupta, "Mc3d: Motion contrast 3d scanning," in *2015 IEEE International Conference on Computational Photography (ICCP)*. IEEE, 2015, pp. 1–10.

[36] S. Herbort, B. Gerken, D. Schugk, and C. Woehler, "3d range scan enhancement using image-based methods," *ISPRS journal of photogrammetry and remote sensing*, vol. 84, pp. 69–84, 2013.

[37] O. Alstad and O. Egeland, "Elimination of Reflections in Laser Scanning Systems with Convolutional Neural Networks," *Modeling, Identification and Control*, vol. 43, no. 1, pp. 9–20, 2022.

[38] D. Goldstein and E. Collett, *Polarized Light, Revised and Expanded*, ser. Optical engineering -New York- Marcel Dekker Incorporated-. Taylor & Francis, 1993.

[39] E. Collett, *Field guide to polarization*. SPIE, 2005.

[40] N. A. Rubin, G. D'Aversa, P. Chevalier, Z. Shi, W. T. Chen, and F. Capasso, "Matrix fourier optics enables a compact full-stokes polarization camera," *Science*, vol. 365, no. 6448, p. eaax1839, 2019.

[41] N. Lefaudeux, N. Lechocinski, S. Breugnot, and P. Clemenceau, "Compact and robust linear stokes polarization camera," in *Polarization: Measurement, Analysis, and Remote Sensing VIII*, vol. 6972. SPIE, 2008, p. 69720B.

[42] Y. Ma, S. Soatto, J. Kosecka, and S. S. Sastry, *An invitation to 3-d vision: from images to geometric models*. Springer, 2012, vol. 26.

[43] R. Gonzalez and R. Woods, *Digital Image Processing*, 4th ed. Pearson, 2018, pp. 154–160.
[44] S. Mihoubi, O. Losson, B. Mathon, and L. Macaire, "Multispectral demosaicing using intensity-based spectral correlation," in *2015 International Conference on Image Processing Theory, Tools and Applications (IPTA)*. IEEE, 2015, pp. 461–466.
[45] C. Kanan and G. W. Cottrell, "Color-to-grayscale: does the method matter in image recognition?" *PloS one*, vol. 7, no. 1, p. e29740, 2012.
[46] W. K. Pratt, *Introduction to digital image processing*. CRC press, 2013, pp. 21–84.
[47] R. W. Schafer, "What is a savitzky-golay filter?[lecture notes]," *IEEE Signal processing magazine*, vol. 28, no. 4, pp. 111–117, 2011.
[48] A. Savitzky and M. J. Golay, "Smoothing and differentiation of data by simplified least squares procedures," *Analytical chemistry*, vol. 36, no. 8, pp. 1627–1639, 1964.
[49] P. A. Gorry, "General least-squares smoothing and differentiation by the convolution (savitzky-golay) method," *Analytical Chemistry*, vol. 62, no. 6, pp. 570–573, 1990.
[50] Z. Gan and Q. Tang, *Visual sensing and its applications: integration of laser sensors to industrial robots*. Springer, 2011.
[51] J. I. Trisnadi, "Speckle contrast reduction in laser projection displays," in *Projection displays VIII*, vol. 4657. SPIE, 2002, pp. 131–137.
[52] T. Okawa, S. Ooki, H. Yamajo, M. Kawada, M. Tachi, K. Goi, T. Yamasaki, H. Iwashita, M. Nakamizo, T. Ogasahara *et al.*, "A 1/2inch 48m all pdaf cmos image sensor using 0.8 μm quad bayer coding 2$\times$ 2ocl with 1.0 lux minimum af illuminance level," in *2019 IEEE International Electron Devices Meeting (IEDM)*. IEEE, 2019, pp. 16–3.
[53] G. Mathers, *The welding of aluminium and its alloys*. Elsevier, 2002.
[54] C. J. Willmott and K. Matsuura, "Advantages of the mean absolute error (mae) over the root mean square error (rmse) in assessing average model performance," *Climate research*, vol. 30, no. 1, pp. 79–82, 2005.
[55] Q. Huynh-Thu and M. Ghanbari, "Scope of validity of psnr in image/video quality assessment," *Electronics letters*, vol. 44, no. 13, pp. 800–801, 2008.

Jaime Marco-Rider (Member, IEEE) received the B.Sc. in Industrial Engineering specializing in Industrial Electronics from the University of Cadiz, Spain. He received the M.Sc. in Electronic Systems and Instrumentation from both Mid Sweden University (MiUN), Sundsvall, Sweden and the Norwegian University of Science and Technology (NTNU), Trondheim, Norway, in 2019.

After several years working in the Spanish industry, he moved to Scandinavia where he started doing research on sensor solutions for industrial robotics applications.

Marco-Rider is currently a PhD Candidate in the Department of Mechanical and Industrial Engineering at NTNU, since 2019.

Andrej Cibicik (Member, IEEE) received the M.Sc. degree in civil engineering from the Technical University of Denmark (DTU), Copenhagen, in 2012. He received the Ph.D degree in mechanical and industrial engineering from the Norwegian University of Science and Technology (NTNU), Trondheim, Norway, in 2020.

From 2012 to 2016 he held industrial positions within structural strength analysis of civil structures and offshore drilling equipment. Currently he is a research scientist at the Dept. of Production Technology in SINTEF Manufacturing, Trondheim, Norway.

His research interests include robotics, production technology, multibody dynamics, automatic control, sensor systems and estimation.

Olav Egeland (Senior Member, IEEE) received the M.Sc. and Ph.D. degrees in automatic control from the Norwegian University of Science and Technology (NTNU), Trondheim, Norway, in 1984 and 1987, respectively.

He was a Professor of robotics within electrical engineering at NTNU from 1989 to 2004. He was a co-founder of a start-up from 2004 to 2011. He is currently a Professor of production automation with the Department of Mechanical and Industrial Engineering, NTNU.

Dr. Egeland received the Automatica Prize Paper Award in 1996 and the IEEE TRANSACTIONS ON CONTROL SYSTEM TECHNOLOGY Outstanding Paper Award in 2000. He was an Associate Editor of the IEEE TRANSACTIONS ON AUTOMATIC CONTROL from 1996 to 1999 and European Journal of Control from 1998 to 2000. His research interest includes modeling and control for robotic and offshore applications.